ADVANCED ELECTRONIC MATERIALS Open Access
www.advelectronicmat.de

Volatile and Nonvolatile Dual-Mode Switching Operations in an Ag-Ag_2S Core-Shell Nanoparticle Atomic Switch Network

*Oradee Srikimkaew, Saverio Ricci, Matteo Porzani, Thien Tan Dang, Yusuke Nakaoka, Yuki Usami, Daniele Ielmini, and Hirofumi Tanaka**

This paper proposes a nanoparticle-based atomic switch network memristive device, capable of both volatile and nonvolatile switching operations, which have not been previously reported for this material. The operational modes can be determined by altering the compliance current, demonstrating high stability over 100 cycles. Analysis of the conduction mechanism using *I–V* curves reveals switching characteristics consistent with space-charge-limited current conduction during the set process and ohmic behavior in the reset state. Furthermore, this study analyzes these dual-operational modes in devices with varying electrode spacings. The results indicate that a wider spacing necessitated a higher compliance current for the volatile-to-nonvolatile transition, underscoring the significance of interconnection. These findings facilitate the integration of neuron and synapse functions within a single atomic switch network device, thereby advancing neuromorphic systems.

1. Introduction

The rapid advancement of artificial intelligence has created a growing demand for intelligent computational approaches. Neuromorphic computing, drawing inspiration from the structure and function of the human brain, offers a promising solution to this demand owing to its capacity for intelligent computing, including energy efficiency, execution speed, real-time processing, and adaptability.[1,2] Neuromorphic architectures often leverage memristive crossbar arrays, capitalizing on their potential to implement large-scale neural networks. Within this framework, individual cross-points serve as artificial neurons and synapses, facilitating parallel communication and information processing.[3,4] However, current memristive crossbar arrays face physical limitations when emulating the topology, interconnectivity, and adaptability of biological neural networks.[5,6] In biological neural networks, neurons are densely interconnected, forming complex networks that facilitate information processing, memory storage, and decision-making. Drawing inspiration from this interconnectivity, nanoarchitectures based on self-organized memristive atomic switch networks (ASNs) have been proposed as alternatives to biologically plausible computing hardware.[7–11] In this approach, emergent behavior arises from the complexity and interactions of atomic switching junctions within the network, rather than relying on individual elements. These switching junctions are the cross-point junctions of nanowires that autonomously organize into a network. They constitute two-terminal circuit elements comprising a memristive material (e.g., polyvinylpyrrolidone, Ag_2S, and TiO_2) sandwiched between metals (e.g., Ag). Materials exhibiting resistive switching characteristics generally operate in volatile or nonvolatile states, depending on the retention characteristics of their resistance states. The low-resistance state (LRS) or high-resistance state (HRS) of a material can persist (nonvolatile) or dissipate (volatile) when the applied voltage is removed. Inspired by brain functions, materials exhibiting volatile switching are primarily employed to emulate integrate-and-fire neuron functions,[12–16] whereas materials exhibiting nonvolatile switching are utilized for replicating synaptic functions.[17–21] However, the successful implementation of a neuromorphic system requires the incorporation of both neuronal and synaptic functionalities in the overall framework.[22]

O. Srikimkaew[+], T. T. Dang, Y. Nakaoka, Y. Usami, H. Tanaka
Graduate School of Life Science and Systems Engineering
Kyushu Institute of Technology (Kyutech)
2–4 Hibikino, Wakamatsu, Kitakyushu 808-0196, Japan
E-mail: tanaka@brain.kyutech.ac.jp

H. Tanaka
School of Physics
Institute of Science
Suranaree University of Technology
Nakhon Ratchasima 30000, Thailand

S. Ricci, M. Porzani, D. Ielmini
Dipartimento di Elettronica
Informazione e Bioingegneria (DEIB)
Politecnico di Milano and IUNET
piazza L. da Vinci 32, Milano 20133, Italy

Y. Usami, H. Tanaka
Research Center for Neuromorphic AI Hardware, Kyutech
Kitakyushu 808-0196, Japan

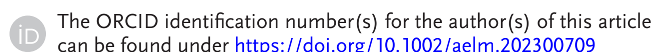
The ORCID identification number(s) for the author(s) of this article can be found under https://doi.org/10.1002/aelm.202300709

[+]Present address: Futuristic Science Research Center, School of Science, Walailak University, Nakhon Si Thammarat 80160, Thailand

© 2024 The Author(s). Advanced Electronic Materials published by Wiley-VCH GmbH. This is an open access article under the terms of the Creative Commons Attribution License, which permits use, distribution and reproduction in any medium, provided the original work is properly cited.

DOI: 10.1002/aelm.202300709

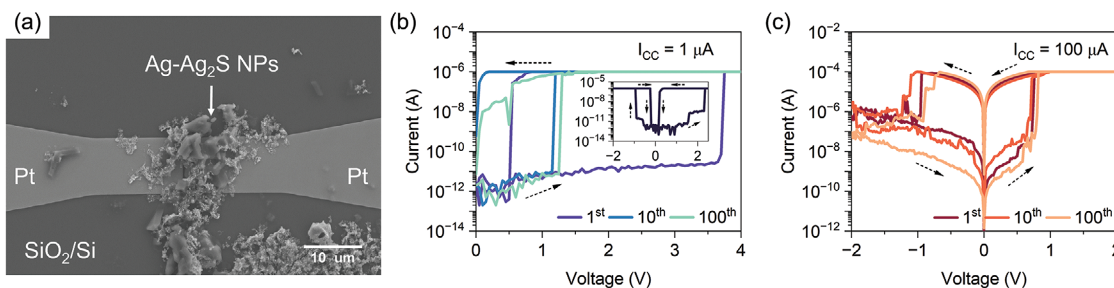

Figure 1. a) SEM image of a planar Pt/Ag-Ag_2S NPs/Pt device with an electrode gap of 1 µm. b) The *I*–*V* characteristics of volatile switching operation under an I_{CC} of 1 µA. The inset shows a bidirectional sweep of volatile switching operated on the same device. c) Nonvolatile switching characteristics under an I_{CC} of 100 µA.

Therefore, the integration of both volatile and nonvolatile functionalities into a single ASN system can expedite the development of neuromorphic applications.

In this study, we experimentally demonstrated volatile and nonvolatile resistive switching in a nanoparticle (NP)-based ASN memristive device, a phenomenon not previously reported for this ASN material. Despite the theoretical[7] and experimental[10,23–31] results already obtained regarding this resistive switching behavior, the precise operation of this dual-functional volatile and nonvolatile switching remains unclear. Consequently, we investigated the resistive switching behavior and determined the operational mode by adjusting the compliance current (I_{CC}). We assessed the cycling endurance of the device, which exhibited high stability over 100 cycles for both volatile and nonvolatile operations. Furthermore, we showed that controlling the transition from volatile to nonvolatile behavior could be achieved by manipulating the electrode spacing of the device. Our results indicate that this NP-based ASN device can offer an integrated system of neuronal and synaptic functions, paving the way for the development of neuromorphic systems.

2. Results and Discussion

2.1. Volatile and Nonvolatile Operations

Figure 1a shows a Pt/Ag-Ag_2S NPs/Pt switching device fabricated as a two-terminal planar structure with 1 µm electrode spacing. The dual-operational resistive switching of the device was investigated by varying the I_{CC}. Current (*I*)–voltage (*V*) characteristics shown in Figure 1b indicate that the device exhibited volatile switching behavior during low-current operation with an I_{CC} of 1 µA. In the first sweep, the device initially remained in the HRS and then transitioned to the LRS at a relatively high set voltage (V_{set} ≈3.7 V). This is because ASN-based switching devices require an activation process (electroforming) before initiating resistive switching behavior.[27,29] As the voltage was reversed, the current adhered to compliance and then spontaneously returned to its original HRS at ≈0.5 V. The return to the original state after voltage removal signifies the nature of volatile switching.[32–34] This volatile switching characteristic persisted after 100 consecutive positive sweeps, indicating high stability during the volatile operation. Moreover, the device exhibits volatile switching properties even during bidirectional sweeps, as shown in the inset of Figure 1b, enabling operation in both directions. In contrast to volatile switching, nonvolatile switching behavior was observed when the device was operated with a high I_{CC} of 100 µA, as shown in Figure 1c. When the voltage was swept in a positive direction, the current increased abruptly at the V_{set} of ≈0.7 V, resulting in the device transitioning from the HRS to the LRS. When the subsequent negative voltage was applied, the device remained in the LRS and switched back to the HRS at a reset voltage (V_{reset}) of ≈−1 V. High switching stability was also achieved during nonvolatile operation, as evidenced by its consistency after 100 cycles of bidirectional sweeping.

One hundred consecutive cycles of volatile and nonvolatile switching were further analyzed, as shown in **Figure** 2a–d and detailed in Figure S1 (Supporting Information). The HRS and LRS resistance values were extracted from *I*–*V* sweep cycles at a reading voltage of 0.4 V. The device switched between the HRS and LRS with a high off-on resistance ratio of ≈10^5 during volatile operation, as shown in Figure 2a. However, overlapping resistance values in the LRS indicated that some sweeping cycles resulted in switching failure. The V_{set} distribution shown in Figure 2b reveals fluctuating V_{set} values during volatile switching. In contrast, the V_{reset} and V_{set} values of nonvolatile switching (Figure 2d) are distributed in the range of −0.5––2 V and concentrated ≈0.7 V, indicating consistent switching across cycles. Figure 2c shows the HRS and LRS values during nonvolatile operation. The resistance of the HRS decreased, resulting in a lower off-on resistance ratio of ≈10^3. Resistance stability was higher in the LRS, whereas it was unstable in the HRS because of the intense local Joule heating that facilitated Ag filament dissolution.[35,36] Uniform nonvolatile switching was also observed across devices, as shown in Figure 2e,f and Figure S2 (Supporting Information). Statistical analysis was conducted using ten switching cycles of five randomly selected devices. The observed characteristics of HRS variation and narrow switching voltage distribution among different devices show consistent trends. However, device number four (D4) exhibited a broad range of V_{set} and V_{reset}, possibly because the Ag-Ag_2S NPs not fully cover the electronic gap, as shown in Figure 2h.

2.2. Conduction Mechanism

To investigate the conduction mechanism in the Pt/Ag-Ag_2S NPs/Pt switching device, the *I*–*V* curves of both volatile and

 © 2024 The Author(s). Advanced Electronic Materials published by Wiley-VCH GmbH

RIGHTSLINK

2199160x, 2024, 10, Downloaded from https://onlinelibrary.wiley.com/doi/10.1002/aelm.202300709 by POLITECNICO DI MILANO, Wiley Online Library on [22/10/2024]. See the Terms and Conditions (https://onlinelibrary.wiley.com/terms-and-conditions) on Wiley Online Library for rules of use; OA articles are governed by the applicable Creative Commons License

2199160x, 2024, 10, Downloaded from https://onlinelibrary.wiley.com/doi/10.1002/aelm.202300709 by POLITECNICO DI MILANO, Wiley Online Library on [22/10/2024]. See the Terms and Conditions (https://onlinelibrary.wiley.com/terms-and-conditions) on Wiley Online Library for rules of use; OA articles are governed by the applicable Creative Commons License

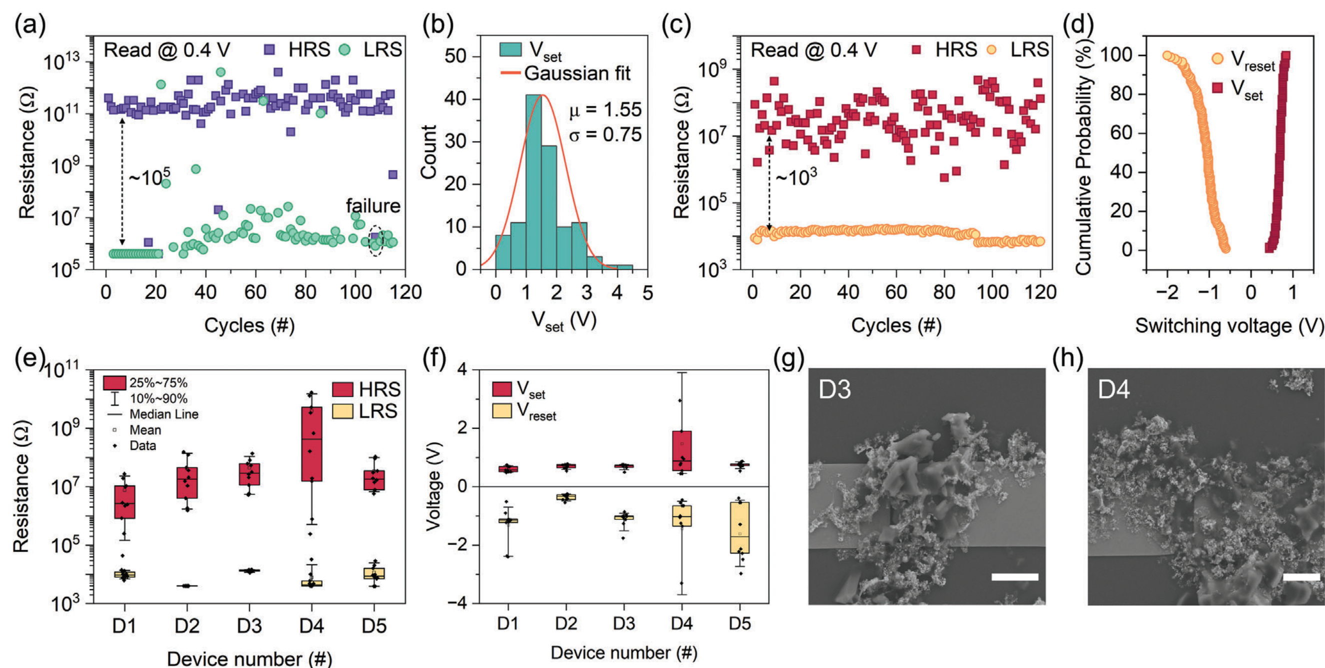

Figure 2. a) Cycle-to-cycle endurance and b) V_{set} distribution of volatile switching acquired from 115 sweeping cycles. c) Cycle-to-cycle endurance and d) cumulative probability plot of V_{reset} and V_{set} of nonvolatile switching obtained from 120 sweeping cycles. Device-to-device statistical assessment of resistance e) and switching voltages f) in nonvolatile switching. Five devices were randomly selected, and each underwent 10 sweeping cycles. g,h) SEM images of devices D3 and D4. The scale bar indicates 5 µm.

nonvolatile behaviors were plotted on a double-logarithmic scale, as shown in **Figure 3**. For nonvolatile behavior during the set process at the HRS (Figure 3a), the *I–V* relationship follows the characteristics of a trap-controlled space-charge-limited current (SCLC).[37–39] The current varies linearly with voltage ($I \propto V$) in the small bias region, followed by higher power dependence ($I \propto V^n$ with $n \geq 1.7$) in the larger bias region. A conductive pathway was formed after the SET process, resulting in the *I–V* relationship presenting ohmic conduction behavior ($I \propto V$) at the LRS, where the slope equals 1. A similar conduction mechanism was observed during the reset process (Figure 3b). The LRS maintained a linear *I–V* relationship, and the SCLC again dominated conduction after the reset process. For volatile operation, the current exhibits a quadratic dependence on voltage ($I \propto V^2$) at the HRS, followed by the set process with a rapid increase in current (Figure 3c). These characteristics are consistent with SCLC conduction.[20,33,38,40] During the self-reset process at the LRS, the device exhibited ohmic conduction behavior (slope of ≈1). The similarities in the *I–V* characteristics of the volatile and nonvolatile switching behaviors suggest that the underlying mechanisms controlling the device operation in both modes are similar.

According to the literature, the switching process in an Ag_2S atomic switch is related to ionic diffusion owing to electrochemical reactions.[41–44] The switching mechanism of the Ag-Ag_2S NP-based ASN can be explained by considering the formation of the Ag filament pathway, as shown in Figure 3d. The paths that allowed the current to flow with the least resistance were selected to form a conductive pathway across the NP network, owing to the minimization of energy dissipation. Because the NPs have a core (Ag)–shell (Ag_2S) structure,[45] the contact area between the two NPs behaves as a metal (Ag)–semiconductor (Ag_2S)–metal (Ag) junction. This junction can function as an atomic switch, forming Ag filaments within the Ag_2S layer via electrochemical reactions.[46–48] During the forward bias in the set process, Ag atoms are oxidized into ions that migrate along the electric field. These ions are reduced to neutral atoms through a reduction reaction by electrons from the opposite direction, resulting in the formation of Ag filaments to bridge the nanojunctions. Once the conductive pathway owing to filament formation is formed across the network, the device switches from the HRS to the LRS. Controlling I_{CC} can affect the volume of the filament formed.[40,49,50] Thin and unstable filaments are expected to be formed when the device undergoes the set process at low I_{CC} (1 µA), as shown in Figure 3e on the left. Such instability of the thin filaments results in the spontaneous dissolution of the Ag filament pathway as the applied voltage is removed (Figure 3e, right), resulting in volatile switching behavior. However, as the I_{CC} increases (100 µA), thick filaments can be formed and remain stable for an extended duration (Figure 3f on the left). The highly conducting state is preserved, and the device is converted into nonvolatile switching. When the reset process is performed during the next negative bias, the Ag atoms that formed the filament are oxidized to ions via an oxidation reaction. This causes the dissolution of the Ag filament pathway, and the device switches back to the HRS, as shown in Figure 3e. The formation of conductive pathways in nanowire (NW)-based atomic switch networks has been demonstrated in previous studies.[51–53] These studies used graph theory to describe the connectivity between multiple NW–NW junctions. Initially, the conductance changes occur near the

 © 2024 The Author(s). Advanced Electronic Materials published by Wiley-VCH GmbH
RIGHTSLINK

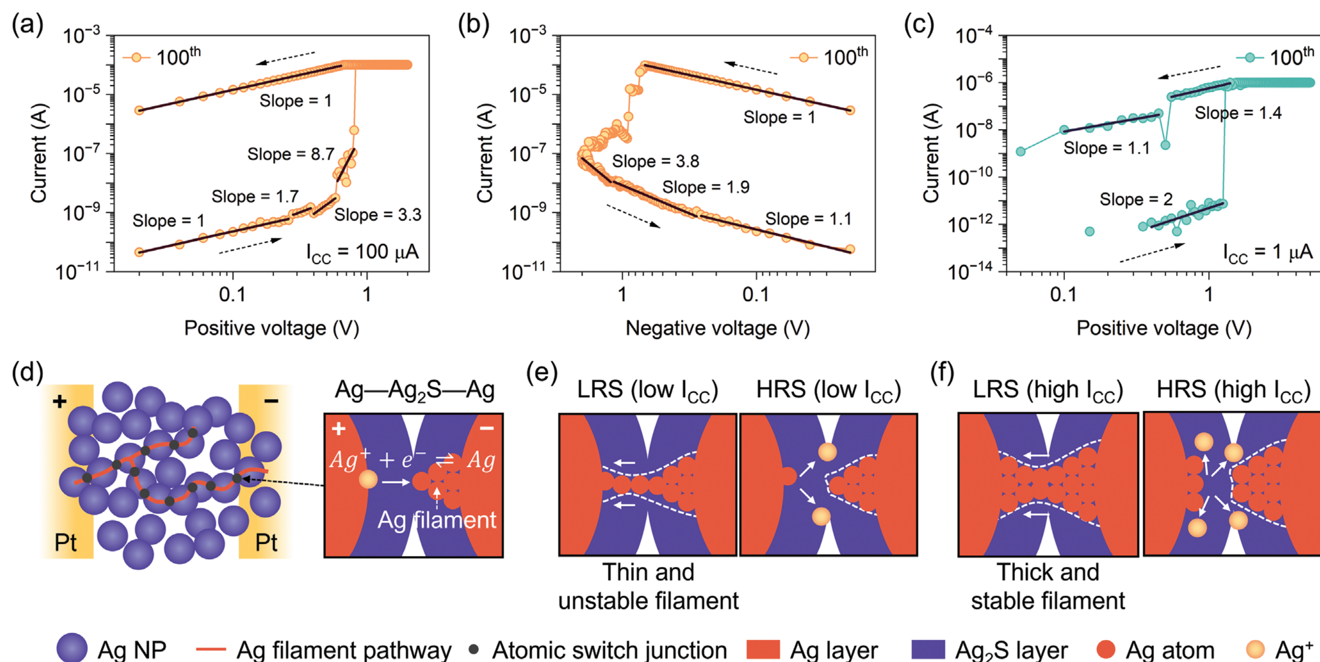

Figure 3. *I–V* curve fitting results of the nonvolatile switching during the set a) and reset b) processes, and volatile switching c). d) Schematic of Ag filament formation across the NP network. The formation and dissolution of the Ag filament at NP contact under low e) and high I_{CC} f).

electrodes, then adjacent junctions are activated sequentially, forming a conductive pathway between the electrodes while minimizing energy dissipation. Such a similar mechanism can be applied to NP networks. Due to the smaller size of NPs compared to NWs, a denser NP network may be necessary to establish a continuous conductive pathway through filament growth between the electrodes.

2.3. Altering Electrode Spacing

Altering the electrode spacing can affect the switching characteristics in a random network configuration.[25,30] To explore the impact of electrode spacing on volatile and nonvolatile operation modes, switching devices with varying electrode spacing ranging from 1 to 10 μm were fabricated. **Figure 4** shows the *I–V* characteristics of the device with varying electrode spacings at different I_{CC} levels. A dual-switching operation was achieved in all devices as the I_{CC} was adjusted. However, the I_{CC} required for the transition from volatile to nonvolatile behavior increased as the electrode spacing increased (Figure 4e). This observed increase in the transition current can be attributed to the formation of a stable conductive path between the electrodes following the set process. When the device is operated with the same I_{CC}, a shorter electrode spacing causes the current to flow and concentrate near the narrow gap between the electrodes, facilitating a higher current density in certain regions. Consequently, a stable conductive pathway likely forms. In contrast, in devices with a wider electrode spacing, the current disperses more widely, resulting in lower current density within specific regions. Thus, the potential for current crowding and the subsequent formation of a stable conductive pathway is reduced. This reduction in the likelihood of forming a stable conductive pathway necessitates increased I_{CC} for a device with a wider electrode spacing to transition from a volatile to a nonvolatile regime.

3. Conclusion

In summary, we demonstrated that volatile and nonvolatile operations can be achieved in a single Ag-Ag_2S NP-based ASN system. During low-current operation with an I_{CC} of 1 μA, the device exhibited volatile switching behavior, while high-current operation at 100 μA resulted in nonvolatile switching behavior. The stability of both volatile and nonvolatile switching modes was assessed over 100 cycles, revealing reliable dual-operational switching performance. Despite some instances of failure, volatile operation achieved a high off-on resistance ratio of 10^5. Nonvolatile switching exhibited uniform switching behavior across cycles and devices, although the off-on resistance ratio slightly reduced to $\approx 10^3$. The conduction mechanism was investigated using *I–V* curves, which showed that both volatile and nonvolatile behaviors exhibited characteristics consistent with trap-controlled SCLC during the set process and ohmic behavior during the reset state. The switching mechanism is attributed to the formation of Ag filament pathways within the Ag_2S layer, involving ionic diffusion through an electrochemical reaction. Lower I_{CC} caused unstable and thin filaments, resulting in volatile behavior, whereas higher I_{CC} facilitated the formation of stable and thicker filaments, leading to nonvolatile behavior. Furthermore, the impact of electrode spacing on the switching characteristics was explored. The results indicate that a wider electrode spacing required a higher I_{CC} to transition from volatile to nonvolatile behavior. This effect can be attributed to the reduced likelihood of forming a stable filament pathway. Our investigation provides

© 2024 The Author(s). Advanced Electronic Materials published by Wiley-VCH GmbH
RIGHTSLINK
2199160x, 2024, 10, Downloaded from https://onlinelibrary.wiley.com/doi/10.1002/aelm.202300709 by POLITECNICO DI MILANO, Wiley Online Library on [22/10/2024]. See the Terms and Conditions (https://onlinelibrary.wiley.com/terms-and-conditions) on Wiley Online Library for rules of use; OA articles are governed by the applicable Creative Commons License

ADVANCED ELECTRONIC MATERIALS
Open Access
www.advelectronicmat.de

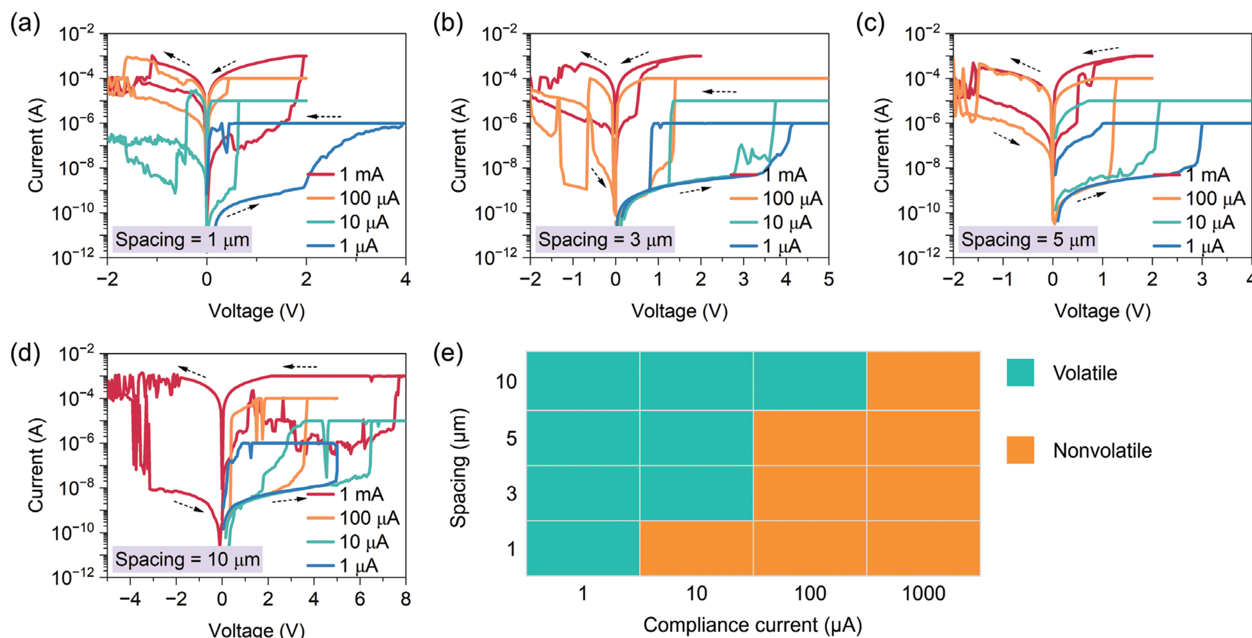

Figure 4. *I–V* curves at different I_{CC} values of the device with electrode spacings of a) 1, b) 3, c) 5, and d) 10 µm. e) The electrode spacing–I_{CC} relationship indicates the threshold for the transition from volatile to nonvolatile behavior.

valuable insights into the operational dynamics of Ag-Ag_2S NP-based ASN devices, encompassing both volatile and nonvolatile behaviors, endurance, conduction mechanisms, and the influence of electrode spacing. These findings enhance our understanding of the capabilities of this device in neuromorphic hardware and computing technology. Additionally, performing quantitative model calculations would offer a more thorough comprehension of the transport mechanisms, which can be further explored in future studies.

4. Experimental Section

Ag-Ag_2S NPs were synthesized using a previously established method.[31,45] The resulting NPs exhibited a core-shell structure with metallic Ag cores surrounded by Ag_2S-like phases. The average diameter of NPs is 38 ± 16 nm with a thickness of the core/shell layer of 18 ± 8/1.0 ± 0.4 nm.[31] To fabricate the Ag-Ag_2S NP-based ASN device, a two-terminal configuration was initially patterned using conventional optical lithography. A SiO_2 (285 nm on Si) substrate was prepared using chemical vapor deposition, and Pt/Ti (35/5 nm) contact electrodes were then deposited on the SiO_2 substrate by thermal evaporation. A suspension of Ag NPs (40 mg/mL in ethanol, volume 40 µL) was subsequently spin-coated onto the electrode at a speed of 500 rpm for 30 s and left to dry at 100 °C for 1 min. The device structure was observed via SEM (LEO1525). *I–V* characterizations were conducted at room temperature using an Agilent HP4156C parameter analyzer and a custom MATLAB program. The switching voltage and resistance values were extracted from the *I–V* curves using MATLAB. Curve-fitting analysis was performed using Origin software.

Supporting Information

Supporting Information is available from the Wiley Online Library or from the author.

Acknowledgements

The authors thank Dr. T. Morimoto in National Institute of Advanced Industrial Science and Technology for fruitful discussion. This work was financially supported by KAKENHI (grant Nos. 21K14527, 22H01900, 23K17864, and 23K18495) JST CREST (grant No. JPMJCR21B5), ACT-X (grant no. JPMJAX22K4), ALCA-Next (Grant No. JPMJAN23F3), and JSPS Core-to-Core Project (Grant No. JPJSCCA20220006). O.S. thanks to support of the Core-to-Core project to stay in Politecnico di Milano for 2 months for collaboration. This work was also supported by Suranaree University of Technology (SUT), Thailand Science Research and Innovation (TSRI), and National Science, Thailand Research and Innovation Fund (NSRF) (NRIIS Project Number 90465). [Correction added on July 13th, 2024, after first online publication: the first author's affiliations have been corrected in this version.]

Conflict of Interest

The authors declare no conflict of interest.

Data Availability Statement

Research data are not shared.

Keywords

atomic switch networks, electrode spacing, nonvolatile, resistive switching, silver–silver sulfide nanoparticles, volatile

Received: October 13, 2023
Revised: May 31, 2024
Published online: July 10, 2024

© 2024 The Author(s). Advanced Electronic Materials published by Wiley-VCH GmbH
RIGHTSLINK
2199160x, 2024, 10, Downloaded from https://onlinelibrary.wiley.com/doi/10.1002/aelm.202300709 by POLITECNICO DI MILANO, Wiley Online Library on [22/10/2024]. See the Terms and Conditions (https://onlinelibrary.wiley.com/terms-and-conditions) on Wiley Online Library for rules of use; OA articles are governed by the applicable Creative Commons License

[1] C. D. Schuman, S. R. Kulkarni, M. Parsa, J. P. Mitchell, P. Date, B. Kay, *Nat. Comput. Sci.* **2022**, *2*, 10.
[2] W. Zhang, B. Gao, J. Tang, P. Yao, S. Yu, M. F. Chang, H. J. Yoo, H. Qian, H. Wu, *Nat. Electron.* **2020**, *3*, 371.
[3] Q. Xia, J. J. Yang, *Nat. Mater.* **2019**, *18*, 309.
[4] D. Ielmini, H. S. P. Wong, *Nat. Electron.* **2018**, *1*, 333.
[5] E. R. Kandel, J. H. Schwartz, T. M. Jessell, S. A. Siegelbaum, A. J. Hudspeth, *Principles of Neural Science*, McGraw Hill, New York **2014**.
[6] L. E. Suárez, R. D. Markello, R. F. Betzel, B. Misic, *Trends Cognit. Sci.* **2020**, *24*, 302.
[7] H. O. Sillin, R. Aguilera, H.-H. Shieh, A. V. Avizienis, M. Aono, A. Z. Stieg, J. K. Gimzewski, *Nanotechnology* **2013**, *24*, 384004.
[8] G. Milano, G. Pedretti, K. Montano, S. Ricci, S. Hashemkhani, L. Boarino, D. Ielmini, C. Ricciardi, *Nat. Mater.* **2022**, *21*, 195.
[9] S. Lilak, W. Woods, K. Scharnhorst, C. Dunham, C. Teuscher, A. Z. Stieg, J. K. Gimzewski, *Front. Nanotechnol.* **2021**, *3*, 675792.
[10] Q. Li, A. Diaz-Alvarez, D. Tang, R. Higuchi, Y. Shingaya, T. Nakayama, *ACS Appl. Mater. Interfaces* **2020**, *12*, 50573.
[11] T. Tsuchiya, T. Nakayama, K. Ariga, *Appl. Phys. Express* **2022**, *15*, 100101.
[12] Q. Duan, Z. Jing, X. Zou, Y. Wang, K. Yang, T. Zhang, S. Wu, R. Huang, Y. Yang, *Nat. Commun.* **2020**, *11*, 3399.
[13] X. Zhang, W. Wang, Q. Liu, X. Zhao, J. Wei, R. Cao, Z. Yao, X. Zhu, F. Zhang, H. Lv, S. Long, M. Liu, *IEEE Electron Device Lett.* **2018**, *39*, 308.
[14] J.-Q. Yang, R. Wang, Z.-P. Wang, Q.-Y. Ma, J.-Y. Mao, Y. Ren, X. Yang, Y. Zhou, S.-T. Han, *Nano Energy* **2020**, *74*, 104828.
[15] B. Xie, X. Zhang, S. Cheng, W. Jie, *Mater. Des.* **2022**, *222*, 111090.
[16] H. Mao, Y. Zhu, S. Ke, Y. Zhu, K. Shi, X. Wang, C. Wan, Q. Wan, *Appl. Phys. Lett.* **2023**, *123*, 013501.
[17] X. Yan, J. Zhao, S. Liu, Z. Zhou, Q. Liu, J. Chen, X. Y. Liu, *Adv. Funct. Mater.* **2018**, *28*, 1705320.
[18] L. Liu, W. Xiong, Y. Liu, K. Chen, Z. Xu, Y. Zhou, J. Han, C. Ye, X. Chen, Z. Song, M. Zhu, *Adv. Electron. Mater.* **2020**, *6*, 1901012.
[19] L. Zhou, J.-Y. Mao, Y. Ren, J.-Q. Yang, S.-R. Zhang, Y. Zhou, Q. Liao, Y.-J. Zeng, H. Shan, Z. Xu, J. Fu, Y. Wang, X. Chen, Z. Lv, S.-T. Han, V. A. L. Roy, *Small* **2018**, *14*, 1800288.
[20] A. Thomas, A. N. Resmi, A. Ganguly, K. B. Jinesh, *Sci. Rep.* **2020**, *10*, 12450.
[21] J. Wang, C. Shi, M. L. Sushko, J. Lan, K. Sun, J. Zhao, X. Liu, X. Yan, *ACS Appl. Mater. Interfaces* **2021**, *13*, 39641.
[22] Z. Wang, S. Joshi, S. Savel'Ev, W. Song, R. Midya, Y. Li, M. Rao, P. Yan, S. Asapu, Y. Zhuo, H. Jiang, P. Lin, C. Li, J. H. Yoon, N. K. Upadhyay, J. Zhang, M. Hu, J. P. Strachan, M. Barnell, Q. Wu, H. Wu, R. S. Williams, Q. Xia, J. J. Yang, *Nat. Electron.* **2018**, *1*, 137.
[23] Y. U. Hadiyawarman, T. Kotooka, S. Azhari, M. Eguchi, H. Tanaka, *Jpn. J. Appl. Phys.* **2021**, *60*, SCCF02.
[24] M. E. Hadiyawarman, H. Tanaka, *Jpn. J. Appl. Phys.* **2020**, *59*, 015001.
[25] A. Diaz-Alvarez, R. Higuchi, P. Sanz-Leon, I. Marcus, Y. Shingaya, A. Z. Stieg, J. K. Gimzewski, Z. Kuncic, T. Nakayama, *Sci. Rep.* **2019**, *9*, 14920.
[26] E. C. Demis, R. Aguilera, K. Scharnhorst, M. Aono, A. Z. Stieg, J. K. Gimzewski, *Jpn. J. Appl. Phys.* **2016**, *55*, 1102B2.
[27] A. Z. Stieg, A. V. Avizienis, H. O. Sillin, C. Martin-Olmos, M.-L. Lam, M. Aono, J. K. Gimzewski, *Jpn. J. Appl. Phys.* **2014**, *53*, 01AA02.
[28] A. Z. Stieg, A. V. Avizienis, H. O. Sillin, C. Martin-Olmos, M. Aono, J. K. Gimzewski, *Adv. Mater.* **2012**, *24*, 286.
[29] A. V. Avizienis, H. O. Sillin, C. Martin-Olmos, H. H. Shieh, M. Aono, A. Z. Stieg, J. K. Gimzewski, *PLoS One* **2012**, *7*, e42772.
[30] P. N. Nirmalraj, A. T. Bellew, A. P. Bell, J. A. Fairfield, E. K. McCarthy, C. O'Kelly, L. F. C. Pereira, S. Sorel, D. Morosan, J. N. Coleman, M. S. Ferreira, J. J. Boland, *Nano Lett.* **2012**, *12*, 5966.
[31] O. Srikimkaew, D. Banerjee, S. Azhari, Y. Usami, H. Tanaka, *ACS Appl. Electron. Mater.* **2023**, *6*, 688.
[32] H. Sun, Q. Liu, C. Li, S. Long, H. Lv, C. Bi, Z. Huo, L. Li, M. Liu, *Adv. Funct. Mater.* **2014**, *24*, 5679.
[33] Y.-J. Huang, S.-C. Chao, D.-H. Lien, C.-Y. Wen, J.-H. He, S.-C. Lee, *Sci. Rep.* **2016**, *6*, 23945.
[34] S. Nirantar, E. Mayes, M. A. Rahman, T. Ahmed, M. Taha, M. Bhaskaran, S. Walia, S. Sriram, *Adv. Electron. Mater.* **2019**, *5*, 1900605.
[35] K. J. Yoon, J. W. Han, D. Il Moon, M. L. Seol, M. Meyyappan, H. J. Kim, C. S. Hwang, *Nanoscale Adv.* **2019**, *1*, 2990.
[36] C. Liang, K. Terabe, T. Hasegawa, M. Aono, *Nanotechnology* **2007**, *18*, 485202.
[37] M. A. Lampert, *Phys. Rev.* **1956**, *103*, 1648.
[38] M. A. Lampert, *Rep. Prog. Phys.* **1964**, *27*, 329.
[39] N. Ilyas, D. Li, C. Li, X. Jiang, Y. Jiang, W. Li, *Nanoscale Res. Lett.* **2020**, *15*, 30.
[40] B. Lu, J. Du, J. Lu, S. Li, R. Yang, P. Liu, J. Huang, L. Chen, F. Zhuge, Z. Ye, *ACS Mater. Lett.* **2023**, *5*, 1350.
[41] T. Hasegawa, K. Terabe, T. Nakayama, M. Aono, *RIKEN Rev.* **2001**, *37*, 7.
[42] K. Terabe, T. Hasegawa, T. Nakayama, M. Aono, *Nature* **2005**, *433*, 47.
[43] A. Nayak, T. Tamura, T. Tsuruoka, K. Terabe, S. Hosaka, T. Hasegawa, M. Aono, *J. Phys. Chem. Lett.* **2010**, *1*, 604.
[44] T. Hasegawa, K. Terabe, T. Tsuruoka, M. Aono, *Adv. Mater.* **2012**, *24*, 252.
[45] C. Battocchio, C. Meneghini, I. Fratoddi, I. Venditti, M. V. Russo, G. Aquilanti, C. Maurizio, F. Bondino, R. Matassa, M. Rossi, S. Mobilio, G. Polzonetti, *J. Phys. Chem. C* **2012**, *116*, 19571.
[46] K. Terabe, T. Nakayama, T. Hasegawa, M. Aono, *J. Appl. Phys.* **2002**, *91*, 10110.
[47] A. Gubicza, D. Z. Manrique, L. Pósa, C. J. Lambert, G. Mihály, M. Csontos, A. Halbritter, *Sci. Rep.* **2016**, *6*, 30775.
[48] Y. Yang, P. Gao, S. Gaba, T. Chang, X. Pan, W. Lu, *Nat. Commun.* **2012**, *3*, 732.
[49] S. K. Vishwanath, H. Woo, S. Jeon, *Nanotechnology* **2018**, *29*, 235202.
[50] J. Woo, H. Hwang, *ECS J. Solid State Sci. Technol.* **2016**, *5*, Q98.
[51] G. Milano, E. Miranda, C. Ricciardi, *Neural Netw.* **2022**, *150*, 137.
[52] A. Loeffler, A. Diaz-Alvarez, R. Zhu, N. Ganesh, J. M. Shine, T. Nakayama, Z. Kuncic, *Sci. Adv.* **2023**, *9*, eadg3289.
[53] R. Zhu, S. Lilak, A. Loeffler, J. Lizier, A. Stieg, J. Gimzewski, Z. Kuncic, *Nat. Commun.* **2023**, *14*, 6697.

© 2024 The Author(s). Advanced Electronic Materials published by Wiley-VCH GmbH

RIGHTSLINK

2199160x, 2024, 10, Downloaded from https://onlinelibrary.wiley.com/doi/10.1002/aelm.202300709 by POLITECNICO DI MILANO, Wiley Online Library on [22/10/2024]. See the Terms and Conditions (https://onlinelibrary.wiley.com/terms-and-conditions) on Wiley Online Library for rules of use; OA articles are governed by the applicable Creative Commons License